Revision #1

Lorenz number and transport properties of Fe: Implications to the thermal conductivity at Earth's core-mantle boundary

Yuan Yin[1,2], Lin Wang[3†], Shuangmeng Zhai[2*], Yun Liu[1,4*]

[1]State Key Laboratory of Ore Deposit Geochemistry, Institute of Geochemistry, Chinese Academy of Sciences, Guiyang 550081, China

[2]Key Laboratory of High-temperature and High-pressure Study of the Earth's Interior, Institute of Geochemistry, Chinese Academy of Sciences, Guiyang 550081, China

[3]Earth and Planets Laboratory, Carnegie Institution for Science, Washington, DC 20015, USA

[4]Research Center for Planetary Science, College of Earth Sciences, Chengdu University of Technology, Chengdu 610059, China

[*]Corresponding authors: Shuangmeng Zhai (zhaishuangmeng@mail.gyig.ac.cn) and Yun Liu (liuyun@vip.gyig.ac.cn)

[†]Present address: Bayerisches Geoinstitut, University of Bayreuth, Bayreuth 95440, Germany.

Highlights:

- Four-wire van der Pauw method is applied in the multi-anvil press to measure the electrical resistivity of solid iron at 300 K and pressures to 26 GPa.
- The thermal conductivity of solid hcp iron is calculated as 129±9 W/m/K at 136 GPa and 300 K conditions by the first-principles molecular dynamics method.
- Electrical resistivity and thermal conductivity of solid hcp iron at Earth's CMB are estimated as ~76-83 μΩ·cm and 114 ± 6 W/m/K, respectively.

This is the peer-reviewed, final accepted version for American Mineralogist, published by the Mineralogical Society of America.
The published version is subject to change. Cite as Authors (Year) Title. American Mineralogist, in press.
DOI: https://doi.org/10.2138/am-2023-9246. http://www.minsocam.org/

Abstract

The electrical resistivity (ρ) and thermal conductivity (κ) of the Earth's core compositions are essential parameters for constraining the core's thermal state, the inner core age, and the evolutionary history of the geodynamo. However, controversies persist between experimental and computational results regarding the electronic transport properties (ρ and κ) of the Earth's core. Iron is the major element in the core, and its transport properties under high pressure and high temperature conditions are crucial for understanding the core's thermal state. We measured the ρ values of solid iron using the four-wire van der Pauw method at 300 K and pressures ranging from 3 to 26 GPa within a multi-anvil press. For comparison, we calculated the ρ and κ values of hexagonal close-packed (hcp) iron at conditions of 300-4100 K and 22-136 GPa using the first-principles molecular dynamics (FPMD) method. Our calculations generally align with prior studies, indicating that the electrical resistivity of solid hcp iron at Earth's core-mantle boundary (CMB) conditions is ~76-83 μΩ·cm. The resistivity of hcp iron changes small as it melts from solid to liquid at pressures from 98 to 134 GPa. The impact of temperature and pressure on the Lorenz numbers of solid hcp iron are investigated according to our calculation results and previous studies. Under the CMB's pressure conditions, the κ of hcp iron initially decreases with increasing temperature and subsequently increases. The electron-electron scattering plays a dominant role at low temperatures and causes the decrease in κ. At high temperatures, the increase of electronic specific heat significantly increases the Lorentz number and κ. Overall, we estimate the κ of solid hcp iron at CMB's condition to be 114 ± 6 W/m/K, slightly lower than the room temperature value of 129±9 W/m/K at the same pressure. Our model shows that a 0-525 km thickness of a

thermally stratified layer may exist beneath the Earth's CMB depending on the core's heat flow and thermal conductivity.

Keywords: iron, first-principles calculation, thermal conductivity, Earth's core, high pressure experiments

This is the peer-reviewed, final accepted version for American Mineralogist, published by the Mineralogical Society of America.
The published version is subject to change. Cite as Authors (Year) Title. American Mineralogist, in press.
DOI: https://doi.org/10.2138/am-2023-9246. http://www.minsocam.org/

INTRODUCTION

The Earth's core consists of Fe, Ni, and light elements like Si, S, O, C, H, and P, as suggested by geochemical and geophysical observations (Li and Fei 2014). The thermal conductivity (κ) of iron, the dominant element in the core, is thus essential to constrain the core's thermal properties, which impact geodynamo models, the age of the inner core, thermal evolution, and the magnetic field over geological time (Davies et al. 2015, 2022; Driscoll and Bercovici 2014; Labrosse 2015; Nimmo 2015). Moreover, since electrons are the primary transport particles in metals, the electrical resistivity (ρ, the reciprocal of electrical conductivity) of iron is related to its electronic thermal conductivity (κ_{el}), described by the Wiedemann-Franz law (WFL), $\kappa_{el} = LT/\rho$, where L is the Lorenz number, and T is the temperature. Though the lattice (ionic) thermal conductivity contributes to the total thermal conductivity of pure iron and iron alloys under the Earth's core-mantle boundary (CMB) conditions, it is approximately 2-5% of the electronic part and is negligible (Pozzo et al. 2012; Yue and Hu 2019). Thus, the resistivity of iron and iron alloys can be used to estimate the thermal properties of the Earth's core, and extensive studies on the resistivity have been conducted through experiments and first-principles calculations based on density functional theory (DFT) (see the reviews of Berrada and Secco 2021; Pommier et al. 2022; Yin et al. 2022a). The DFT method usually calculates electronic part of thermal conductivity through the Chester-Thellung formulation of the Kubo-Greenwood formula (Chester and Thellung 1961; Greenwood 1958; Kubo 1957) and ionic contribution with the Green-Kubo formula (Kubo 1957). Furthermore, due to the significant challenge in the experiment, only a few studies have reported the thermal conductivity of iron and iron alloys measured in-situ at high pressure-temperature (P-T)

conditions (Hasegawa et al. 2019; Hsieh et al. 2020; Konôpková et al. 2016; Saha et al. 2020).

The thermal conductivity of the Earth's core remains debated. Resistivity measurements and the first-principles calculations both suggest that the Earth's CMB has a high thermal conductivity (~100 W/m/K) (Gomi et al. 2016; Li et al. 2022; Pozzo et al. 2012; Seagle et al. 2013; Xu et al. 2018; Zhang et al. 2022). Nevertheless, thermal conductivity measurement experiments indicate a low κ value of ~20-30 W/m/K at the CMB (Hsieh et al. 2020; Konôpková et al. 2016). The low thermal conductivity in the core implies a low rate of heat transfer by conduction, which can sustain a long-lived thermal dynamo and extend the onset time of inner core solidification to ~3.4 Ga ago (Gomi et al. 2013; Hsieh et al. 2020; Konôpková et al. 2016). Conversely, high thermal conductivity in the core corresponds to a rapid cooling rate and a high initial temperature at the CMB, implying that the solidification of the inner core started less than 1 Ga ago (Li et al. 2022). Pozzo et al. (2022) attempted to reconcile experimental and computational transport properties of Fe-Si alloys at high *P-T* conditions via the DFT calculation method. Compared to experimental results (Hsieh et al. 2020), their calculated thermal conductivity with electron-electron scattering (EES) correction matches the experiments at 72-106 GPa but exceeds at 121-144 GPa.

As the high *P-T* resistivity of iron samples in most experiments (Inoue et al. 2020; Ohta et al. 2023; Zhang et al. 2020) is computed based on room-temperature data, this room-temperature information is a vital benchmark. The resistivity of iron at room temperature varies between studies. Previous measurements indicate that the highest resistivity of hexagonal-close-packed (hcp) iron at ~20 GPa and 300 K was ~24 μΩ·cm (Gomi et al.

100 2013; Jaccard et al. 2002; Yong et al. 2019), nearly twice of the results (13 μΩ·cm) from
101 recent measurements (Ezenwa and Yoshino 2021; Zhang et al. 2020). One reason for this
102 discrepancy is the systematic uncertainty in estimating sample thickness under high
103 pressure conditions (Lobanov and Geballe 2022). With the DFT method, Gomi et al.
104 (2013) and Sha and Cohen (2011) calculated the resistivity of hcp iron at room
105 temperature and high pressure conditions using the ordered lattice structures, yielding
106 results deduced at 0 K, coming with lower resistivity values than experiments at 20-80
107 GPa. Moreover, Xu et al. (2018) calculated the electronic transport properties of hcp iron
108 under Earth's core conditions, including the electron-lattice scattering and the EES
109 contribution. However, they omitted the thermal disorder effect and did not address the
110 room temperature situation. Zhang et al. (2020) calculated the resistivity of hcp iron at
111 105 GPa and 2000 K, incorporating the thermal disorder effect and EES effect, aligning
112 with the experimental data. In some studies (Pozzo et al. 2014, 2022; Pozzo and Alfè
113 2016), the thermal disorder effect was included in the calculations for solid hcp iron and
114 iron-silicon alloys, but no discussions on the room temperature conditions.

115 The Wiedemann-Franz law connects electrical resistivity and electronic thermal
116 conductivity through the Lorentz number. Based on the assumption that WFL relies on
117 elastic electron scattering (Klemens and Williams 1986; Uher 2004), Lorentz number has
118 a Sommerfeld theoretical value (L_0) of 2.445×10^{-8} $W\Omega K^{-2}$. The inelastic scattering of
119 electrons in thermal conduction makes the Lorentz number deviate from the L_0. A
120 systematic investigation on the Lorenz number for iron and iron-silicon alloys under high
121 *P-T* conditions was conducted by Secco (2017), revealing that the Lorenz number
122 positively deviates from L_0 when the electronic component fails to fully describe the total

thermal conductivity. This departure was observed in pure Fe and Fe-Si alloys under ambient pressure and high temperature conditions (Secco 2017). Under high pressures, the inelastic scattering of electrons is enhanced with rising temperature, causing the Lorenz number to fall below L_0 (Secco 2017). As a result, the Lorenz number exhibits variability under high *P-T* conditions (Pozzo et al. 2022). Experimental results (Konôpková et al. 2016; Zhang et al. 2020) roughly suggest that the Lorentz number of hcp iron at 80-200 GPa and 2000-3000 K is about 0.8-1.0×10^{-8} WΩK^{-2} (Yin et al. 2022a), significantly lower than L_0. Even in the case of a Fermi liquid with only inelastic scattering, the L value of hcp iron under Earth's core conditions is 1.59×10^{-8} WΩK^{-2}, about 0.65L_0 (Pourovskii et al. 2017), which still exceeds experimental observations. Gomi and Yoshino (2018) calculated the Lorentz number of iron-light elements (Si, Ni, S, C, N, and O) alloys under high *P-T* conditions, suggesting that the species and concentration of light elements significantly affect the Lorentz number, particularly under high temperature conditions. Liquid Fe-Si-O alloys exhibit smaller Lorentz numbers than pure iron, indicating that light elements can decrease the L values (Pozzo et al. 2013). In addition, Pourovskii et al. (2020) theoretically calculated the L value at Earth's core conditions for the perfect hcp iron lattice at 1.57×10^{-8} WΩK^{-2} and for the thermo-disordered one at 2.28×10^{-8} WΩK^{-2}. However, there are limited reports on the Lorenz number of iron under room temperature conditions.

To comprehensively understand the temperature and pressure effects on the electronic transport properties of iron, we applied both experiments and the first-principles calculation method in this study. Though the resistivity of iron has been widely measured and discussed in the multi-anvil press experiments, most previous studies used the

conventional four-wire method for resistivity measurement (Ezenwa and Yoshino 2021; Secco and Schloessin 1989; Yong et al. 2019). The four-wire van der Pauw method is broadly employed in diamond-anvil cell experiments to measure the resistivity of iron and iron alloys (Gomi et al. 2013; Seagle et al. 2013; Zhang et al. 2020). For comparison, we used the van der Pauw method to measure the resistivity of iron at room temperature (300 K) and pressures from 3 to 26 GPa in the multi-anvil press. To broaden the pressure and temperature range, we calculated the electrical resistivity of hcp iron at both room temperature and high temperature conditions (300-4100 K and 22-136 GPa). Most previous studies only used ordered lattice structures to calculate the electronic transport properties of solid hcp iron at 300 K (Gomi et al. 2013; Sha and Cohen 2011) and high temperature conditions (Xu et al. 2018). In this study, we applied the first-principles molecular dynamics (FPMD) method and the Kubo-Greenwood formula (Greenwood 1958; Kubo 1957). The FPMD method generates disordered lattice structures and naturally includes the thermal disorder effect. Using the Chester-Thellung-Kubo-Greenwood approach (Chester and Thellung 1961), we also estimated the electronic thermal conductivity. Based on the results, we discussed the temperature and pressure effect on the Lorentz number and transport properties of hcp iron at high *P*-*T* conditions. These results are also applied to constrain the thermal conductivity in the Earth's core, subsequently used to estimate the adiabatic heat flow in the core, inner core age, and the thermally stratified layer thickness beneath the CMB.

METHODS AND CALCULATIONS

Electrical resistivity measurement of iron

This is the peer-reviewed, final accepted version for American Mineralogist, published by the Mineralogical Society of America.
The published version is subject to change. Cite as Authors (Year) Title. American Mineralogist, in press.
DOI: https://doi.org/10.2138/am-2023-9246. http://www.minsocam.org/

All experiments were conducted at room temperature (300 K) and 3-26 GPa in an 800-ton multi-anvil press in the Earth and Planets Laboratory at Carnegie Institute for Science. For high pressure studies, we used an 8/3 assembly, in which the Cr_2O_3-doped MgO octahedron has an 8 mm length edge, and tungsten carbide has a 3 mm length corner-truncated edge. An iron plate sample with a thickness of 0.5 mm and a diameter of 1.6 mm was sandwiched by two Al_2O_3 rods and placed at the center of the assembly. Additionally, two MgO bars were placed on top of Al_2O_3 rods to serve as pressure transition materials. The 8/3 assembly sketch is shown in Figure S1 in the supporting information. For the resistivity measurements, we utilized a four-wire van der Pauw method (van der Pauw 1958) and used four tungsten wires (a diameter of 0.1 mm) as leads to measure sample's resistance. The van der Pauw method requires the contact point between the wire and the sample to be as small as possible to minimize errors. Our tungsten wires were much smaller than the sample size, and the contact area at the iron plate's edge was also small. It is crucial to ensure that the sample had a flat shape with uniform thickness and was homogeneous and isotropic. Our sample, a pure iron plate, meets these requirements. Controlling sample deformation and thickness during the experiment presented challenges, but we used two Al_2O_3 rods to minimize the impact of deformation. Figure S1 shows no significant deformation was observed in the recovered samples.

The measurement strategy is similar to our previous study (Yin et al. 2022b). We first press the sample to the target pressure, hold the pressure, and then start resistance measurement. All resistance data are acquired during the compression process. However, due to experimental challenges, only two runs yielded reasonable data. The U1419 run

192 reached a maximum pressure of 22.3 GPa before the tungsten leads broke at higher
193 pressures. In the U1423 run, no data was recorded below 13 GPa due to lead
194 disconnection. The pressure uncertainty is 0.5 GPa in our experiments. After experiments,
195 the recovered samples were mounted in epoxy resin and subsequently ground and
196 polished to measure the sample's thickness. The iron plate sample had a thickness of 0.5
197 mm before the experiment and 0.39-0.43 mm after the experiment (Figure S1). With
198 these post-compression dimensions (sample thickness) and measured resistances at 300 K,
199 we calculated the resistivity at different pressure conditions. As the Al_2O_3 rods are much
200 harder than pure iron, we neglected the volume change during decompression. The
201 change in thickness of the iron plates during compression was estimated using an
202 equation of the state for pure iron (Zhang and Guyot, 1999). The total estimation of
203 resistivity error is from the geometry uncertainty and is less than 4% in our experiments.

204

205 **First-principles calculations**

206 The electronic transport properties of iron at 300-4100 K and 22-136 GPa were
207 calculated using FPMD and the Kubo-Greenwood formula in the Computational
208 Geochemistry Lab at the Institute of Geochemistry, Chinese Academy of Sciences.
209 Calculations were carried out using the Vienna Ab initio Simulation Packages (VASP), a
210 plane wave density functional code developed by Kresse and Furthmüller (1996), and
211 incorporated the projector augmented wave (PAW) method (Blöchl 1994; Kresse and
212 Jouber, 1999) to represent ion-electron interaction. The potential file is the Perdew,
213 Burke, and Ernzerhof (Perdew et al. 1996) type ($3p^6 4s^1 3d^7$ valence configuration,
214 labelled PAW_PBE Fe_pv), and the plane-wave cutoff energy is 400 eV (similar to Li et

al. 2022 and Wagle et al. 2018). The supercells of the hcp Fe have 150 atoms, comparable to the literature (Li et al. 2022; Pourovskii et al. 2020; Wagle et al. 2018). The unit cell's lattice parameters were derived from high pressure X-ray diffraction experiments in the literature (Anzellini et al. 2013; Dewaele et al. 2006; Fei et al. 2016) (Table S1). For comparison, additional calculations for hcp iron were conducted using the calculated lattice parameters at 0 K, which displayed comparable *c/a* ratios to previous theoretical studies (Kleinschmidt et al. 2023; Pourovskii et al. 2014). Figure S2 shows that the *c*/*a* ratios calculated by the DFT method at 0 K are smaller than the experimental results at 300 K. Kleinschmidt et al. (2023) suggested that the electronic transport properties of hcp iron are insensitive to the *c/a* ratios under high temperature conditions. However, the impact of *c/a* ratios under room temperature conditions remains unclear. Volume is a significant parameter in the Kubo-Greenwood formula, and thermal expansion influences the volume under high temperatures. Thus, we exclusively used the experimental lattice parameter to construct supercells at high temperatures ranging from 1500 to 4100 K. Then, we employed FPMD with the canonical ensemble (NVT: number of atoms, volume, and temperatures are constant) to update the atomic coordinates of the supercell at a time step of 1 fs. Temperature is controlled by the Nosé-Hoover thermostat (Hoover 1985; Nosé 1984). The FPMD simulation ran for 11 ps, with the first ps discarded for equilibration, and one snapshot of nuclear positions was extracted every 500 molecular dynamic steps from the final 5 ps. The electronic states were occupied according to Fermi-Dirac statistics at the thermostat's temperature, and only the gamma point was used to sample the Brillouin zone during molecular dynamics simulations.

This is the peer-reviewed, final accepted version for American Mineralogist, published by the Mineralogical Society of America.
The published version is subject to change. Cite as Authors (Year) Title. American Mineralogist, in press.
DOI: https://doi.org/10.2138/am-2023-9246. http://www.minsocam.org/

Using a VASP post-processing tool, KG4VASP (Di Paola et al. 2020), we calculated the electrical resistivity through the Kubo-Greenwood formula (Greenwood 1958; Kubo 1957) and electronic thermal conductivity with the Chester-Thellung-Kubo-Greenwood formula (Chester and Thellung 1961). The electrical and thermal conductivities are derived as the frequency in Onsager coefficients in the above formulas approach zero (Di Paola et al. 2020). Like Korell et al. (2019), we employed a linear extrapolation method when the frequency equals zero as the results usually unphysically decrease at very small frequencies. For every snapshot, we used a dense grid of 4x4x4 *k*-points in the Gamma centered scheme, which ensured convergence in calculations. The Dirac delta functions were approximated with one Gaussian function with a spreading of 10 meV, minimizing its value to remove the small oscillations in the optical conductivity arising from the discretization of the band structure. After calculation, we averaged ρ and κ_{el} over the snapshots and considered one standard deviation as the uncertainty. In this study, the electronic transport properties were calculated at the DFT level, including electron-lattice scattering, while the EES was disregarded. Given the computational cost and its slight impact on results at pressures above 50 GPa (Korell et al. 2019), the spin polarization effect was also neglected. The Lorenz number ($L=k_{el}*\rho/T$) was determined through the WFL based on our electrical and thermal conductivity results.

RESULTS AND DISCUSSIONS

Electrical resistivity of hcp Fe

This is the peer-reviewed, final accepted version for American Mineralogist, published by the Mineralogical Society of America.
The published version is subject to change. Cite as Authors (Year) Title. American Mineralogist, in press.
DOI: https://doi.org/10.2138/am-2023-9246. http://www.minsocam.org/

In Figure 1a, we present the results of our experimental measurements of iron's electrical resistivity under conditions of 3-26 GPa and 300 K, alongside our theoretical calculation results at 22-136 GPa and 300 K. Figure 1a also includes the previous experimental results (Ezenwa and Yoshino 2021; Gomi et al. 2013; Jaccard et al. 2002; Seagle et al. 2013; Ohta et al. 2023; Zhang et al. 2018, 2020) and theoretical calculation results (Gomi et al. 2013; Sha and Cohen 2011). When the pressure increases from 3 to 11 GPa, the iron's resistivity decreases, followed by a rapid increase from 11 to 19 GPa. Then, resistivity decreases once again as the pressure rises from 19 to 26 GPa (Figure 1a). The inflection point in resistivity at 11 GPa is due to the phase transition of iron from bcc to hcp phase, ending at 19 GPa. Within the 11-19 GPa range, the sample is a mixture of bcc and hcp phases. Our results are roughly consistent with those of Ezenwa and Yoshino (2021), who measured the bcc to hcp phase transition pressure range between 12-20 GPa. Our results align with Seagle et al. (2013) and Zhang et al. (2020) within the range of uncertainties. However, it is worth noting that, below 5 GPa, the results from Ezenwa and Yoshino (2021) were significantly larger than those of this study and Zhang et al. (2020). In the study by Ezenwa and Yoshino (2021), iron probes were used for resistivity measurements, while we used tungsten probes, which are also used and discussed in other studies (Silber et al. 2018; Berrada et al. 2021). The diffusion of probe material into the sample impacts resistivity measurements under high temperature conditions. Given that our experiments were conducted at room temperature, such influence is negligible. The sample deformation and measurement approach may contribute to the variations between the results of Ezenwa and Yoshino (2021) and this study. The highest resistivity of hcp iron measured in this study is about 14.1-15.3 μΩ·cm at 300 K, consistent with certain

281 literature results (Ezenwa and Yoshino 2021; Zhang et al. 2020), but lower than others
282 (Gomi et al. 2013; Jaccard et al. 2002; Zhang et al. 2018). Therefore, the electrical
283 resistivity of hcp iron at 300 K and pressures below 60 GPa may not be as high as some
284 previous estimations (Figure 1a).

285 In comparison with the results by Sha and Cohen (2011) and Gomi et al. (2013), our
286 calculated ρ values for hcp iron at 22-136 GPa and 300 K are generally consistent with
287 experiments (Figure 1a). Notably, in Figure 1a, the R2 simulation (solid down triangle)
288 employed experimental lattice parameters at 300 K from the literature, while the R1
289 simulation (solid up triangle) used the optimized lattice parameters to the lowest energy
290 at 0 K, based on DFT calculations. Though these runs exhibit rough consistency below 80
291 GPa, discrepancies emerge at 80-136 GPa. This is probably due to the different c/a ratios
292 of hcp structure between the experimental data and calculations (Figure S2). Korell et al.
293 (2019) found that spin-polarization impacts the electronic transport properties of liquid
294 iron at 20-50 GPa, which may also impact the solid hcp iron. Pourovskii et al. (2014)
295 indicated that the contribution of EES to the resistivity of hcp iron is ~5% of the total
296 resistivity at 20 GPa and 294 K, and the contribution decreases with increasing pressures.
297 In this study, our calculated results at 20-60 GPa have slightly lower resistivity and much
298 higher thermal conductivity values than experiments (Figure 1). It is possibly due to the
299 omission of spin-polarization and EES effects, both of which tend to increase resistivity
300 and decrease thermal conductivity under high P-T conditions (Korell et al. 2019;
301 Pourovskii et al. 2020).

302 Moreover, we conducted resistivity calculations for hcp iron at high P-T conditions,
303 including 98 GPa (1562 K and 3521 K), 132 GPa (2725 K), and 134 GPa (4114 K). The

304 results are shown in Figure 2a and Table 1. Generally, our results agree with both the
305 experimental data (Zhang et al. 2020) and calculation results (Korell et al. 2019; Xu et al.
306 2018; Zhang et al. 2020). Xu et al. (2018) used ordered lattice structures for simulation,
307 applied a parallel resistor correction for resistivity saturation, and included the EES effect.
308 In Figure 2a, the resistivity calculated by Xu et al. (2018) is slightly higher than ours,
309 likely due to the inclusion of the EES effect. No remarkable resistivity saturation is
310 observed in hcp iron below 134 GPa and 4114 K (Figure 2a). The electrical resistivity of
311 hcp iron shows a quasi-linear temperature dependence in both computational and
312 experimental configurations, suggesting conformability with the Bloch-Grüneisen
313 formula. Our results are also consistent with the calculation results from Korell et al.
314 (2019) under conditions of 135 GPa and 3700 K, indicating a negligible impact from the
315 spin-polarization effect in such conditions. In a recent experimental study, resistivity
316 measurements were conducted for liquid iron at pressures up to 140 GPa (Ohta et al.
317 2023). Figure 2a illustrates that liquid iron at 105 and 135 GPa has slightly higher
318 resistivities than solid hcp iron at 98 and 134 GPa. This implies that the transition from
319 solid hcp iron to a liquid state may not significantly increase the resistivity at
320 pressures >105 GPa. According to previous DFT calculations, the resistivity of hcp iron
321 only experiences a minor increase of 6-10 % upon melting under Earth's core conditions
322 (Pozzo et al. 2014, 2012; Xu et al. 2018).

323

324 **Thermal conductivity of hcp Fe**

325 Figure 1b shows our computed thermal conductivity of hcp Fe with previous
326 experimental (Hsieh et al. 2020; Ohta et al. 2018) and computational results

(Kleinschmidt et al. 2023). Hsieh et al. (2020) measured the thermal conductivity of bcc and hcp iron at 1-120 GPa and 300 K using the time-domain thermoreflectance (TDTR) technique, a well-established ultrafast metrology method that accurately measures the thermal conductivity of materials under high pressure conditions. The thermal conductivity of iron first increases from 76 to 88 W/m/K as pressure increases from 1 to 13 GPa, then rapidly decreases to ~55 W/m/K at 22 GPa. This value remains nearly constant between 22 and 45 GPa, subsequently increasing to 120 ± 30 W/m/K as pressure rises from 45 to 120 GPa (Figure 1b). Compared to the results from Hsieh et al. (2020), Ohta et al. (2018) reported similar κ values at 40-45 GPa but markedly lower values at 16-24 GPa. They employed thermal diffusivity, density, and isobaric heat capacity to calculate thermal conductivity (Ohta et al. 2018), and the observed discrepancies in κ values at ~20 GPa may be attributed to uncertainties arising from heat capacity. The markable change in the thermal conductivity at 13 GPa is a consequence of the phase transition from bcc to hcp Fe (Figure 1b). The low and nearly constant experimental thermal conductivity at 22-45 GPa is possibly due to the electronic topological transition of pure Fe (Glazyrin et al. 2013).

Compared to the experimental data, our calculated κ values for hcp iron are higher at 22-80 GPa but consistent at 80-105 GPa and 300 K (Figure 1b). In Figure 1b, the electronic thermal conductivity in the R1 simulation decreases from 134 to 86 W/m/K as the pressure increases from 60 to 136 GPa, while that of the R2 simulation increases from 116 to 129 W/m/K as the pressure increases from 50 to 136 GPa (Table 1). However, at room temperature, the total thermal conductivity of hcp iron increases with increasing pressure from 80 to 136 GPa (Hsieh et al. 2020). The unexpected decrease of thermal

conductivity in R1 simulation is due to its lattice parameter that was derived at 0 K by DFT calculations. The increase of resistivity between 80-136 GPa in R1 simulation, as shown in Figure 1a, makes it expected in the decrease of thermal conductivity. Therefore, the experimental lattice structures (R2) are more suitable than those (R1) derived from DFT calculations at 0 K for estimating the electronic transport properties of iron under room temperature conditions. At 22-60 GPa, we observe that the calculated resistivity is slightly lower than that in experiments, but the calculated thermal conductivity is much higher. This difference is likely due to disregarding EES and spin-polarization effects during calculation. At 300 K and pressures higher than 50 GPa, the EES and spin-polarization effects become very small (Korell et al. 2019, Pourovskii 2014). Under high *P-T* conditions, the spin-polarization effect impacts resistivity and thermal conductivity almost equally (Korell et al. 2019), while EES affects thermal conductivity more than resistivity (Pourovskii et al. 2020). Hence, the EES effect may have a dominant impact within the pressure range of 22-60 GPa at 300 K. Above 80 GPa, the pressure dependence of hcp iron's thermal conductivity on the isotherm of 1850 K reported by Kleinschmidt et al. (2023) agrees with our result at 300 K (Figure 1b). Overall, our results estimate the κ for hcp iron as 129 ± 9 W/m/K at 136 GPa and 300 K (Table 1).

Konôpková et al. (2016) suggested that the thermal conductivity of hcp iron at the Earth's CMB conditions is as low as 35-55 W/m/K. Figure 2b shows that the electronic thermal conductivity of hcp iron at 2725-4114 K and 132-134 GPa, similar to CMB conditions, is 130-158 W/m/K, nearly three times of the experimental results. The EES significantly affects the electronic transport properties of pure Fe and Fe-Si alloys (Pourovskii et al. 2014, 2020; Zhang et al. 2022). The EES contribution to the total resistivity of hcp iron

increases quasi-linearly from 0 to 28.5% as the temperature increases from 300 to 4000 K at 110-150 GPa (see Figure S7 in the study by Zhang et al. (2022)). Under the Earth's core conditions (360 GPa and 5802 K), including the EES effect, the electrical resistivity of solid hcp iron increased by 9%, and the thermal conductivity decreased by 24% (Pourovskii et al. 2020). Though thermal disorder is the dominant contribution to total scattering, the impact of inelastic scattering from EES cannot be discarded (Pourovskii et al. 2020). Our FPMD calculation method naturally includes the thermal disorder effect but lacks the EES effect. Here we assume that the impact of EES on the electronic thermal conductivity of solid hcp iron at Earth's CMB conditions is temperature-dependent (Xu et al. 2018; Zhang et al. 2022) and increases linearly from 0 to 28.5% as temperature rises from 300 to 4000 K (Figure S3). As mentioned above, EES impacts thermal conductivity more than electrical resistivity. Thus, our assumption may underestimate the EES effect at Earth's CMB condition.

With the EES correction, the thermal conductivity of hcp iron in this study at 98-136 GPa and high temperatures is accordingly reduced to somewhere roughly aligns with the results of the DFT study by Xu et al. (2018), who also accounted for the EES effect in their calculations (Figure 2b). Above all, the EES correction is essential in the calculation of solid iron's thermal conductivity, particularly under high temperature conditions. Figure 2b illustrates that, at 105-136 GPa, the electronic thermal conductivity of hcp iron first decreases with increasing temperature from 300 to ~2000-3000 K and then gradually increases as the temperature rises to 4000 K. In contrast, experiments directly measuring the thermal conductivity suggest that the temperature dependence of the pure hcp iron's thermal conductivity follows a $T^{1/2}$ relationship (Konôpková et al. 2016) at CMB

conditions, deviating significantly from the predicted trend from calculations (Figure 2b). To explain such low thermal conductivity of hcp iron in the experiment, apart from the EES effect, stronger inelastic scattering mechanisms are required to reduce electronic thermal conductivity. At 106-134 GPa and ~1800 K, our calculated results match the upper boundary of thermal conductivity of iron measured by Saha et al. (2020) (Figure 2b). Overall, solid hcp iron's electronic thermal conductivity (with EES correction) at 134 GPa and 4100 K is calculated as 114 ± 6 W/m/K, consistent with previous studies (Xu et al. 2018; Zhang et al. 2020).

Lorenz number of hcp Fe

We computed the total Lorentz number of iron at room temperature through the electrical resistivity (Seagle et al. 2013; Zhang et al. 2020) and thermal conductivity (Hsieh et al. 2020), both directly measured in experiments. We only considered the contribution from thermal conductivity on the uncertainty of the total Lorentz number, as the errors for the experimental resistivity measurement are smaller than those of the thermal conductivity measurement. We have shown that our experimental and calculated results are partly consistent with those measured in the literature (Hsieh et al. 2020; Seagle et al. 2013; Zhang et al. 2020). It remains reasonable to compare the Lorentz number calculated from these literature data with our calculation results, despite large uncertainty arising from different data sources. In Figure 3a, an experimental Lorentz number is as low as ~1.50 $\times 10^{-8}$ WΩK^{-2} at 22-55 GPa and 300 K, smaller than the L_0, indicating a significant inelastic scattering effect in this pressure range. The Lorentz number at pressures between 20 and 50 GPa experiences a drop. It is possibly because the resistivity of hcp

419 iron decreases largely in this pressure range, while the thermal conductivity remains
420 consistent and lower than our calculations based on the assumption of elastic electron
421 scattering. Strong inelastic electron scattering processes can cause the L value to
422 negatively depart from L_0 (Secco 2017). The EES effect induces strong inelastic electron
423 scattering in hcp iron at a pressure range of 22-55 GPa and 300 K and causes the
424 remarkably lower Lorentz numbers compared to L_0 and calculated results from this study.
425 Above 50 GPa, the experimental Lorentz number gradually increases to ~2.3×10^{-8} WΩK^{-2}
426 and remains relatively constant at higher pressures. Pourovskii et al. (2020) calculated
427 the Lorentz number for a perfect lattice structure of solid hcp iron, with $L = 1.57\times10^{-8}$
428 WΩK^{-2}, while for the disordered lattice structure, $L = 2.28\times10^{-8}$ WΩK^{-2}. At 300 K and
429 below 60 GPa, the calculated Lorentz number in this study varies from 2.59 to 2.73×10^{-8}
430 WΩK^{-2}, exceeding both the L_0 and experimental values (Figure 3a; Table 1). At 300 K
431 and 80-136 GPa, the calculated Lorentz number is in the range of 2.1-2.3×10^{-8} WΩK^{-2}
432 (Figure 3a, Table 1), lower than the L_0 value but consistent with experiments.

433 Under 110-190 GPa and 2000-3000 K conditions, Xu et al. (2018) reported the L value of
434 hcp iron as 2.1 $\times10^{-8}$ WΩK^{-2}. As the EES effect on the hcp iron's electrical resistivity is
435 temperature-dependent suggested by Zhang et al. (2022), we accordingly reduce 0-28.5%
436 from the calculated Lorentz number of hcp iron in this study, as shown in Figure 3b,
437 resulting in consistent data with Xu et al. (2018). Pourovskii et al. (2017) indicated that
438 the fraction of EES is enhanced with increasing temperature, and the L value of hcp iron
439 under inner core's pressure conditions decreases from L_0 to ~$0.65L_0$ (1.59×10^{-8} WΩK^{-2},
440 representing the pure Fermi liquid result) as temperatures rise from 300 to 30000 K
441 (Figure 3b, black short dot line). Additionally, Gomi and Yoshino (2018), considering

ordered lattice structures (no thermal disorder and EES effect), calculated the Lorentz number of pure iron and iron alloys. Their results indicate a similar positive temperature-dependence of hcp iron's Lorentz number as the temperatures increase from 300 to 4000 K at 120 GPa (black short dash line in Figure 3b). The inset graph in Figure 3b demonstrates that the Lorentz number (with EES correction) of hcp iron decreases with increasing temperatures from 300 to 2000-3000 K and then increases with increasing temperatures to 4000 K at 98-140 GPa. Under high *P*-*T* conditions, the total Lorentz numbers derived from experimental studies by Zhang et al. (2020), Saha et al. (2020), and Konôpková et al. (2016) are as low as ~0.8 $\times 10^{-8}$ WΩK^{-2}, which seems unreasonable because it is much lower than the case of pure Fermi liquid (1.59×10^{-8} WΩK^{-2}) with only inelastic scattering (Pourovskii et al. 2017) (Figure 3a). It is essential to acknowledge that the total Lorentz numbers derived from non-internal experiments exhibit considerable uncertainty under high-temperature conditions, which could potentially lead to unreasonable interpretations.

As shown in Figure 2b, the computed κ of hcp Fe at 105-136 GPa initially decreases with increasing temperature and subsequently increases. The main reason is the total Lorentz number. In the case of a constant Lorentz number for pure metals, $\kappa \propto T/\rho$. The residual resistivity (ρ_0) causes the rapid decrease in κ at temperatures below 1000 K, as $\rho = \rho_0 + AT$ (Williams, 1998). At high temperatures, $\rho \approx AT$, thus κ approaches to a constant. However, the total Lorentz number, *L(T)* is a function of temperature. When the slope of *L(T)* is positive, the κ will increase with increasing temperature at high temperatures. This is the case in this work and the study of Gomi et al. (2018). Including the EES effect, the *L* values are reduced to below the Sommerfeld value (L_0) (Figure 3b). However, the *L* is

proportional to the electronic specific heat, and the high-order terms of the electronic specific heat cause the deviation of L from the L_0 (Gomi et al., 2015). For hcp iron, below ~2000 K, both numerical and Sommerfeld values of the electronic specific heat show similar linear T-dependences (Boness et al., 1986), suggesting a small slope of L. In this temperature range, the EES effect increases faster than the L as rising temperatures, indicating an EES dominant effect and thus a decrease in κ. But above ~2000 K, the numerical values increase more rapidly than the Sommerfeld value (Gomi et al., 2018) (Figure 3b, S4). Thus, the slope of L becomes larger than that of EES, increasing κ. In comparison to Gomi et al. (2018), our L values are smaller due to the thermal disorder effect (Figure. 3b), but the slope of L under high temperatures is indeed large enough to increase the κ. In summary, the thermal disorder effect systematically reduces the L of hcp iron, the EES effect reduces the L with a linear T-dependence, and the increase of electronic specific heat rapidly enlarges the L at high temperatures.

IMPLICATIONS

Thermal conductivity at the Earth's CMB

At 134 GPa and 4100 K, the thermal conductivity of hcp iron without EES correction is about 158 ± 8 W/m/K, much higher than 100 ± 10 W/m/K estimated by Zhang et al. (2020) and ~97 W/m/K computed by Xu et al. (2018). After EES correcting, the thermal conductivity is reduced to 114 ± 6 W/m/K. Pozzo et al. (2022) pointed out that resistivity saturation may occur for hcp iron above 3000 K. However, our data shows no obvious resistivity saturation for hcp iron from 1500 to 4100 K (Figure 2a). Xu et al. (2018)

computed the saturation resistivity of hcp-Fe under the conditions of the Earth's outer core (136 GPa) and inner core (360 GPa) to be 155 and 143 μΩ·cm, respectively, using the criterion mean free path. At 134 GPa and 4100 K, the computed and experimental resistivity of hcp iron is about 80 μΩ·cm, far below the saturation resistivity (Figure 2a). Thus, no apparent resistivity saturation for hcp iron is found in this study. Using the real-time formalism of time-dependent DFT method, Ramakrishna et al. (2023) calculated the electrical resistivity of hcp iron at conditions related to Earth's core. They detected no apparent resistivity saturation, even at temperature as high as 6000 K.

With the WFL, we estimated the thermal conductivity of hcp iron at the Earth's CMB conditions according to the Bloch-Grüneisen fit data for the resistivity (Figure 2a) from Zhang et al. (2020) and Lorentz numbers (Figure 3b) from this study. As show in the inset of Figure 3b, the Lorentz number varies around 2.20 $\times 10^{-8}$ WΩK^{-2} (0.9 times of L_0), depending on the temperature and pressure. We set the L value of hcp iron to vary from 2.0 to 2.4 $\times 10^{-8}$ WΩK^{-2} at the CMB conditions. The short-dashed lines and grey regions in Figure 2b show the estimation of thermal conductivity at 105 and 136 GPa and temperatures of 300-4100 K. Thus, we estimated the thermal conductivity of solid hcp iron at Earth's CMB conditions as 106-127 W/m/K (136 GPa and 4100 K). The upper boundary of thermal conductivity measured by Saha et al. (2020) falls into the estimated range. After correcting the potential thickness errors of iron samples in the experiments, Lobanov and Geballe (2022) revised the thermal conductivity of hcp iron as 133 W/m/K at Earth's CMB conditions, slightly higher than our estimations. For liquid iron at Earth's CMB conditions, its thermal conductivity could be lower at ~95-114 W/m/K because the electrical resistivity of solid hcp iron may increase ~6-10 % at the onset of melting

(Figure 2a) (Yin et al. 2022a). Furthermore, the lattice thermal conductivity of an iron-rich liquid outer core is about 2.5-4 W/m/K, which is negligible compared to the electronic thermal conductivity (Pozzo et al., 2012). The light elements, such as silicon and oxygen, in the Earth's liquid outer core can also lower the thermal conductivity of iron. With the EES correction (~24% reduction on the κ) to the calculated thermal conductivity of the Fe-Si (Pozzo et al. 2022) and Fe-Ni-O (Li et al. 2022) system, the thermal conductivity at the Earth's CMB is estimated as ~75-85 W/m/K. Therefore, we suggest that the reasonable thermal conductivity at the Earth's CMB is likely from 70 to 90 W/m/K.

Stable thermal stratification

The thermal state of Earth's outer core depends on the core compositions, CMB temperature, and thermal conductivity (Nimmo 2015). The adiabatic heat flow (Q_{ad}) in the core can be approximately computed through the formula:

$$Q_{ad} = -4\pi r^2 \kappa \frac{T_{ad}}{dr} \quad (1)$$

where r is the radius, κ is the thermal conductivity, $\frac{T_{ad}}{dr}$ is the adiabatic temperature gradient. The adiabatic temperature gradient at CMB is about 0.9-1.0 K/km (Davies et al. 2015; Labrosse 2015). Here we simply assumed that the total heat flow in the core (Q_T) is also a function of radius, so that:

$$Q_T = Q_{cmb} = -4\pi r^2 \kappa \frac{dT}{dr} \quad (2)$$

530 which is a good approximation for the heat flow near the CMB (Q_{cmb}). When the
531 uppermost core is subadiabatic, $Q_{cmb} < Q_{ad}$, a thermal stratification layer may exist
532 beneath the CMB (Davies 2015; Nimmo 2015; Zhang et al. 2022). Here, we calculated
533 the adiabatic heat flow across the CMB, ranging from 13.7 TW (with κ = 90 W/m/K) to
534 10.7 TW (with κ = 70 W/m/K), by assuming a 1.0 K/km adiabatic temperature gradient at
535 the topmost of outer core. The present-day total heat flow across the lowermost mantle is
536 estimated at ~10-12 TW according to the thermal conductivity (~10 W/m/K) and
537 temperature gradient data for the lowermost mantle (Okuda et al. 2020). Given the low
538 thermal conductivity of liquid silicate under CMB conditions (~5.3 W/m/K, Deng and
539 Stixrude 2021), the present-day Q_{cmb} may be reduced to 6-7 TW. Davies et al. (2022)
540 employed numerical geodynamo simulations with theoretical scaling laws to propose that
541 a present-day Q_{cmb} in the range of 12-16 TW best aligns with the model for the
542 evolutionary history of Earth's magnetic field strength. However, Frost et al. (2022)
543 suggest a Q_{cmb} of ~15 TW derived from reasonable historic mantle temperatures. In the
544 models from Li et al. (2022), the core's entropy remains positive throughout Earth's
545 history when Q_{cmb} exceeds 7 TW, supporting the existence of the geomagnetic field
546 beginning at 3.5 Ga ago.

547 In the case of high thermal conductivity (111.68-182.33 W/m/K) in the core, Li et al.
548 (2022) calculated the inner core's age in a range from 0.502 to 1.221 Ga (Figure 4).
549 Pozzo et al. (2022), based on a low thermal conductivity of 75-81 W/m/K at Earth's
550 CMB and considering radiogenic heating contribution with 30 ppm ^{40}K in the core,
551 estimated the inner core's age as 0.4-0.8 Ga. Davies et al. (2015) proposed that
552 subadiabatic condition could result in the formation of a thermally stratified layer,

553 potentially hundreds of kilometers thick and stable against thermal convection, beneath
554 the CMB. Using the same approach as Zhang et al. (2022) and assuming the potential
555 thermal conductivity of ~70-90 W/m/K at the CMB, we calculated the thickness of the
556 stratified layer at various Q_{cmb} values (Figure 4). All the parameters used for this
557 calculation are listed in Table S2. When Q_{cmb} is below 13.7 TW, thermal stratification
558 can occur, with its thickness varying from 0 to 1000 km as Q_{cmb} further decreases to 7
559 TW. Notably, thermal stratification is not feasible at the uppermost of the liquid core
560 when Q_{cmb} exceeds ~15 TW. When the Q_{cmb} ranges from 10 to 12 TW, the stratified layer
561 may have a thickness between 0 and 525 km (Figure 4). Similarly, Davies and
562 Greenwood (2023) suggested that the maximum thickness of the thermal stratification
563 layer ranges from 400 to 500 km when the thermal conductivity at the CMB is about 70
564 W/m/K. However, instead of thermal stratification, chemical stratification may play a
565 pivotal role. For instance, a compositional stratification layer may form via chemical
566 interactions between the liquid core and mantle (Buffet and Seagle 2010; Davies et al.
567 2020). Experiments conducted under high *P-T* conditions have revealed the liquid-liquid
568 immiscibility in the Fe-S-H system occurs at pressures up to 118 GPa, providing a
569 scenario of chemical stratification to explain the low-velocity layer beneath the CMB
570 (Yokoo et al. 2022).

571

572 **CONCLUSIONS**

573 We investigated the electrical resistivity of hcp iron at high pressures and room
574 temperature conditions, using both the experimental and first-principles calculation
575 methods. At 136 GPa and 300 K, the electrical resistivity and thermal conductivity of hcp

iron are calculated at 5.72 ± 0.65 μΩ·cm and 129 ± 9 W/m/K, respectively. At 134 GPa and 4100 K, they are 79.58 ± 3.59 μΩ·cm and 114 ± 6 W/m/K, respectively. At 98-136 GPa and 300-4100 K, the Lorentz number of hcp iron varies with pressure and temperature. Based on the resistivity results and Lorentz number, we estimated the thermal conductivity of solid hcp iron at 105 and 136 GPa via the Wiedemann-Franz law. Thus, solid hcp iron at Earth's CMB conditions (136 GPa and 4100 K) has an electronic thermal conductivity of 106-127 W/m/K. Considering the impact of light elements and melting, the corresponding thermal conductivity at CMB decreases to ~70-90 W/m/K. Therefore, a potential subadiabatic condition in the outer core could form a thermally stratified layer with a thickness of 0-525 km beneath the CMB, depending on the current total heat flow across the CMB.

Most of our data reconcile the experimental and computational results for the resistivity and thermal conductivity of solid hcp iron at high pressure and room temperature conditions. However, to explain the abnormally low thermal conductivity of hcp iron at 20-60 GPa and 300 K, further calculations involving the EES and spin-polarization effects are necessary, though these calculations are expensive. Additionally, it's essential to note that the experimental Lorentz number of pure iron in this study was not derived from internal measurement studies. Consequently, future works should focus on generating internally consistent experimental datasets, encompassing electrical resistivity and thermal conductivity, to gain a comprehensive understanding of the Lorentz number for iron and iron alloys under high *P*-*T* conditions. The overall picture of the transport properties of iron from room to high temperature conditions suggests that the liquid outer

598 core has possible low thermal conductivity only if there are a large number of light
599 elements in the outer core.

600

601 ## ACKNOWLEDGEMENTS

602 We are grateful for the critical and constructive comments from four anonymous
603 reviewers that improved the quality of the manuscript. The authors thank Yingwei Fei,
604 Jill Yang, and Joseph Lai at the Carnegie Institution for Science for experimental support,
605 and Yining Zhang and Caihong Gao at the Institute of Geochemistry, CAS for
606 computational assistance. Some of the calculations in this paper are performed on the
607 TianHe-2 supercomputer.

608

609 ## FUNDING

610 This work was financially supported by the National Natural Science Foundation of
611 China (Grant No. 42120104005, 42130114), the UCAS Joint PhD Training Program, the
612 Special Assistant Researcher Grant Project, the International Partnership Program of
613 Chinese Academy of Sciences (Grant No. 132852KYSB20200011), and Guizhou
614 Provincial 2021 Science and Technology Subsidies (Grant No. GZ2021SIG).

615 **References cited**

616 Anzellini, S., Dewaele, A., Mezouar, M., Loubeyre, P., and Morard, G. (2013) Melting of
617 iron at Earth's inner core boundary based on fast x-ray diffraction. Science, 340,
618 464–466, https://doi.org/10.1126/science.1233514.
619 Berrada, M., and Secco, R.A. (2021) Review of electrical resistivity measurements and
620 calculations of Fe and Fe-alloys relating to planetary cores. Frontiers in Earth
621 Science, 9, 1–21, https://doi.org/10.3389/feart.2021.732289.
622 Berrada, M., Secco, R.A., and Yong, W. (2021) Adiabatic heat flow in Mercury's core
623 from electrical resistivity measurements of liquid Fe-8.5 wt%Si to 24 GPa. Earth
624 and Planetary Science Letters, 568, 117053–117053,
625 https://doi.org/10.1016/j.epsl.2021.117053.
626 Blöchl, P.E. (1994) Projector augmented-wave method. Physical Review B, 50, 17953–
627 17979, https://doi.org/10.1103/PhysRevB.50.17953.
628 Boness, D.A., Brown, J.M., and McMahan, A.K. (1986) The electronic thermodynamics
629 of iron under Earth core conditions. Physics of the Earth and Planetary Interiors,
630 42, 227–240, https://doi.org/10.1016/0031-9201(86)90025-7.
631 Buffett, B.A., and Seagle, C.T. (2010) Stratification of the top of the core due to chemical
632 interactions with the mantle. Journal of Geophysical Research: Solid Earth, 115,
633 2009JB006751, https://doi.org/10.1029/2009JB006751.
634 Chester, G.V., and Thellung, A. (1961) The Law of Wiedemann and Franz. Proceedings
635 of the Physical Society, 77, 1005–1013, https://doi.org/10.1088/0370-
636 1328/77/5/309.

637 Davies, C.J. (2015) Cooling history of Earth's core with high thermal conductivity.
638 Physics of the Earth and Planetary Interiors, 247, 65–79,
639 https://doi.org/10.1016/j.pepi.2015.03.007.
640 Davies, C.J., and Greenwood, S. (2023) Dynamics in Earth's core arising from thermo-
641 chemical interactions with the mantle. In T. Nakagawa, T. Tsuchiya, M. Satish-
642 Kumar and G. Helffrich, Ed., Core-Mantle Co-Evolution: An Interdisciplinary
643 Approach, p. 219-258. American Geophysical Union, U.S.
644 https://doi.org/10.1002/9781119526919.ch12.
645 Davies, C.J., Pozzo, M., Gubbins, D., and Alfè, D. (2015) Constraints from material
646 properties on the dynamics and evolution of Earth's core. Nature Geoscience, 8,
647 678–685, https://doi.org/10.1038/ngeo2492.
648 Davies, C.J., Pozzo, M., Gubbins, D., and Alfè, D. (2020) Transfer of oxygen to Earth's
649 core from a long-lived magma ocean. Earth and Planetary Science Letters, 538,
650 116208, https://doi.org/10.1016/j.epsl.2020.116208.
651 Davies, C.J., Bono, R.K., Meduri, D.G., Aubert, J., Greenwood, S., and Biggin, A.J.
652 (2022) Dynamo constraints on the long-term evolution of Earth's magnetic field
653 strength. Geophysical Journal International, 228, 316–336,
654 https://doi.org/10.1093/gji/ggab342.
655 Deng, J., and Stixrude, L. (2021) Thermal conductivity of silicate liquid determined by
656 machine learning potentials. Geophysical Research Letters, 48, e2021GL093806,
657 https://doi.org/10.1029/2021GL093806.

Dewaele, A., Loubeyre, P., Occelli, F., Mezouar, M., Dorogokupets, P.I., and Torrent, M. (2006) Quasihydrostatic equation of state of Iron above 2 Mbar. Physical Review Letters, 97, 29–32, https://doi.org/10.1103/PhysRevLett.97.215504.

Di Paola, C., Macheda, F., Laricchia, S., Weber, C., and Bonini, N. (2020) First-principles study of electronic transport and structural properties of $Cu_{12}Sb_4S_{13}$ in its high-t. Physical Review Research, 2, 033055–033055, https://doi.org/10.1103/PhysRevResearch.2.033055.

Driscoll, P., and Bercovici, D. (2014) On the thermal and magnetic histories of Earth and Venus: Influences of melting, radioactivity, and conductivity. Physics of the Earth and Planetary Interiors, 236, 36–51, https://doi.org/10.1016/j.pepi.2014.08.004.

Ezenwa, I.C., and Yoshino, T. (2021) Martian core heat flux: Electrical resistivity and thermal conductivity of liquid Fe at Martian core P-T conditions. Icarus, 360, 114367, https://doi.org/10.1016/j.icarus.2021.114367.

Fei, Y., Murphy, C., Shibazaki, Y., Shahar, A., and Huang, H. (2016) Thermal equation of state of hcp-iron: Constraint on the density deficit of Earth's solid inner core. Geophysical Research Letters, 43, 6837–6843, https://doi.org/10.1002/2016GL069456.

Frost, D.A., Avery, M.S., Buffett, B.A., Chidester, B.A., Deng, J., Dorfman, S.M., Li, Z., Liu, L., Lv, M., and Martin, J.F. (2022) Multidisciplinary constraints on the thermal-chemical boundary between Earth's core and mantle. Geochemistry, Geophysics, Geosystems, 23, e2021GC009764, https://doi.org/10.1029/2021gc009764.

680 Glazyrin, K., Pourovskii, L.V., Dubrovinsky, L., Narygina, O., McCammon, C., Hewener,
681 B., Schünemann, V., Wolny, J., Muffler, K., Chumakov, A.I., and others (2013)
682 Importance of correlation effects in hcp iron revealed by a pressure-induced
683 electronic topological transition. Physical Review Letters, 110, 117206–117206,
684 https://doi.org/10.1103/PhysRevLett.110.117206.
685 Gomi, H., and Hirose, K. (2015) Electrical resistivity and thermal conductivity of hcp
686 Fe–Ni alloys under high pressure: Implications for thermal convection in the
687 Earth's core. Physics of the Earth and Planetary Interiors, 247, 2–10,
688 https://doi.org/10.1016/j.pepi.2015.04.003.
689 Gomi, H., and Yoshino, T. (2018) Impurity resistivity of fcc and hcp fe-based alloys:
690 Thermal stratification at the top of the core of super-earths. Frontiers in Earth
691 Science, 6, 1–22, https://doi.org/10.3389/feart.2018.00217.
692 Gomi, H., Hirose, K., Akai, H., and Fei, Y. (2016) Electrical resistivity of substitutionally
693 disordered hcp Fe–Si and Fe–Ni alloys: Chemically-induced resistivity saturation
694 in the Earth's core. Earth and Planetary Science Letters, 451, 51–61,
695 https://doi.org/10.1016/j.epsl.2016.07.011.
696 Gomi, H., Ohta, K., Hirose, K., Labrosse, S., Caracas, R., Verstraete, M.J., and Hernlund,
697 J.W. (2013) The high conductivity of iron and thermal evolution of the Earth's
698 core. Physics of the Earth and Planetary Interiors, 224, 88–103,
699 https://doi.org/10.1016/j.pepi.2013.07.010.
700 Greenwood, D.A. (1958) The Boltzmann equation in the theory of electrical conduction
701 in metals. Proceedings of the Physical Society, 71, 585–596,
702 https://doi.org/10.1088/0370-1328/71/4/306.

Hasegawa, A., Yagi, T., and Ohta, K. (2019) Combination of pulsed light heating thermoreflectance and laser-heated diamond anvil cell for in-situ high pressure-temperature thermal diffusivity measurements. Review of Scientific Instruments, 90, 074901, https://doi.org/10.1063/1.5093343.

Hoover, W.G. (1985) Canonical dynamics: Equilibrium phase-space distributions. Physical Review A, 31, 1695–1697, https://doi.org/10.1103/PhysRevA.31.1695.

Hsieh, W.P., Goncharov, A.F., Labrosse, S., Holtgrewe, N., Lobanov, S.S., Chuvashova, I., Deschamps, F., and Lin, J.F. (2020) Low thermal conductivity of iron-silicon alloys at Earth's core conditions with implications for the geodynamo. Nature Communications, 11, 1–7, https://doi.org/10.1038/s41467-020-17106-7.

Inoue, H., Suehiro, S., Ohta, K., Hirose, K., and Ohishi, Y. (2020) Resistivity saturation of hcp Fe-Si alloys in an internally heated diamond anvil cell: A key to assessing the Earth's core conductivity. Earth and Planetary Science Letters, 543, 116357–116357, https://doi.org/10.1016/j.epsl.2020.116357.

Jaccard, D., Holmes, A.T., Behr, G., Inada, Y., and Onuki, Y. (2002) Superconductivity of ε-Fe: Complete resistive transition. Physics Letters, Section A: General, Atomic and Solid State Physics, 299, 282–286, https://doi.org/10.1016/S0375-9601(02)00725-9.

Kleinschmidt, U., French, M., Steinle-Neumann, G., and Redmer, R. (2023) Electrical and thermal conductivity of fcc and hcp iron under conditions of the Earth's core from ab initio simulations. Physical Review B, 107, 085145, https://doi.org/10.1103/PhysRevB.107.085145.

Klemens, P.G., and Williams, R.K. (1986) Thermal conductivity of metals and alloys. International Materials Reviews, 31, 197–215, https://doi.org/10.1179/095066086790324294.

Konôpková, Z., McWilliams, R.S., Gómez-Pérez, N., and Goncharov, A.F. (2016) Direct measurement of thermal conductivity in solid iron at planetary core conditions. Nature, 534, 99–101, https://doi.org/10.1038/nature18009.

Korell, J.-A., French, M., Steinle-Neumann, G., and Redmer, R. (2019) Paramagnetic-to-diamagnetic transition in dense liquid iron and its influence on electronic transport properties. Physical Review Letters, 122, 086601, https://doi.org/10.1103/PhysRevLett.122.086601.

Kresse, G., and Furthmüller, J. (1996) Efficient iterative schemes for ab initio total-energy calculations using a plane-wave basis set. Physical Review B, 54, 11169–11186, https://doi.org/10.1103/PhysRevB.54.11169.

Kresse, G., and Joubert, D. (1999) From ultrasoft pseudopotentials to the projector augmented-wave method. Physical Review B, 59, 1758–1775, https://doi.org/10.1103/PhysRevB.59.1758.

Kubo, R. (1957) Statistical-mechanical theory of irreversible processes. I. General theory and simple applications to magnetic and conduction problems. Journal of the Physical Society of Japan, 12, 570–586, https://doi.org/10.1143/JPSJ.12.570.

Labrosse, S. (2015) Thermal evolution of the core with a high thermal conductivity. Physics of the Earth and Planetary Interiors, 247, 36–55, https://doi.org/10.1016/j.pepi.2015.02.002.

Li, J., and Fei, Y. (2014) Experimental constraints on core composition. In H.D. Holland and K.K. Turekian, Ed., Treatise on Geochemistry (Second Edition), p. 527–557. Elsevier, Oxford. https://doi.org/10.1016/B0-08-043751-6/02014-4.

Li, W.J., Li, Z., He, X.T., Ma, Z., Fu, Z.G., Lu, Y., Wang, C., and Zhang, P. (2022) Ab initio calculations on thermal conductivity of Fe-Ni-O fluid: Constraints on the thermal evolution of Earth's core. Earth and Planetary Science Letters, 589, 117581, https://doi.org/10.1016/j.epsl.2022.117581.

Lobanov, S.S., and Geballe, Z.M. (2022) Non-isotropic contraction and expansion of samples in diamond anvil cells: Implications for thermal conductivity at the core-mantle boundary. Geophysical Research Letters, 49, e2022GL100379, https://doi.org/10.1029/2022GL100379.

Nimmo, F. (2015) Energetics of the Core. In G. Schubert, Ed., Treatise on Geophysics (Second Edition), p. 27–55. Elsevier, Oxford.

Nosé, S. (1984) A unified formulation of the constant temperature molecular dynamics methods. The Journal of Chemical Physics, 81, 511–519, https://doi.org/10.1063/1.447334.

Ohta, K., Nishihara, Y., Sato, Y., Hirose, K., Yagi, T., Kawaguchi, S.I., Hirao, N., and Ohishi, Y. (2018) An experimental examination of thermal conductivity anisotropy in hcp iron. Frontiers in Earth Science, 6, 176, https://doi.org/10.3389/feart.2018.00176.

Ohta, K., Suehiro, S., Kawaguchi, S.I., Okuda, Y., Wakamatsu, T., Hirose, K., Ohishi, Y., Kodama, M., Hirai, S., and Azuma, S. (2023) Measuring the electrical resistivity

of liquid iron to 1.4 Mbar. Physical Review Letters, 130, 266301, https://doi.org/10.1103/PhysRevLett.130.266301.

Okuda, Y., Ohta, K., Hasegawa, A., Yagi, T., Hirose, K., Kawaguchi, S.I., and Ohishi, Y. (2020) Thermal conductivity of Fe-bearing post-perovskite in the Earth's lowermost mantle. Earth and Planetary Science Letters, 547, 116466, https://doi.org/10.1016/j.epsl.2020.116466.

Perdew, J.P., Burke, K., and Ernzerhof, M. (1996) Generalized gradient approximation made simple. Physical Review Letters, 77, 3865–3868, https://doi.org/10.1103/PhysRevLett.77.3865.

Pommier, A., Driscoll, P.E., Fei, Y., and Walter, M.J. (2022) Investigating metallic cores using experiments on the physical properties of liquid iron alloys. Frontiers in Earth Science, 10, 956971, https://doi.org/10.3389/feart.2022.956971.

Pourovskii, L.V., Mravlje, J., Ferrero, M., Parcollet, O., and Abrikosov, I.A. (2014) Impact of electronic correlations on the equation of state and transport in ε -Fe. Physical Review B, 90, 1–5, https://doi.org/10.1103/PhysRevB.90.155120.

Pourovskii, L.V., Mravlje, J., Georges, A., Simak, S.I., and Abrikosov, I.A. (2017) Electron–electron scattering and thermal conductivity of ϵ -iron at Earth's core conditions. New Journal of Physics, 19, 073022–073022, https://doi.org/10.1088/1367-2630/aa76c9.

Pourovskii, L.V., Mravlje, J., Pozzo, M., and Alfè, D. (2020) Electronic correlations and transport in iron at Earth's core conditions. Nature Communications, 11, 5–12, https://doi.org/10.1038/s41467-020-18003-9.

Pozzo, M., and Alfè, D. (2016) Saturation of electrical resistivity of solid iron at Earth's core conditions. SpringerPlus, 5, 1–6, https://doi.org/10.1186/s40064-016-1829-x.

Pozzo, M., Davies, C., and Alfè, D. (2022) Towards reconciling experimental and computational determinations of Earth's core thermal conductivity. Earth and Planetary Science Letters, 584, 117466, https://doi.org/10.1016/j.epsl.2022.117466.

Pozzo, M., Davies, C., Gubbins, D., and Alfè, D. (2012) Thermal and electrical conductivity of iron at Earth's core conditions. Nature, 485, 355–358, https://doi.org/10.1038/nature11031.

Pozzo, M., Davies, C., Gubbins, D., and Alfè, D. (2013) Transport properties for liquid silicon-oxygen-iron mixtures at Earth's core conditions. Physical Review, 87, 1–10, https://doi.org/10.1103/PhysRevB.87.014110.

Pozzo, M., Davies, C., Gubbins, D., and Alfè, D. (2014) Thermal and electrical conductivity of solid iron and iron-silicon mixtures at Earth's core conditions. Earth and Planetary Science Letters, 393, 159–164, https://doi.org/10.1016/j.epsl.2014.02.047.

Ramakrishna, K., Lokamani, M., Baczewski, A., Vorberger, J., and Cangi, A. (2023) Electrical conductivity of iron in Earth's core from microscopic Ohm's law. Physical Review B, 107, 115131, https://doi.org/10.1103/PhysRevB.107.115131.

Saha, P., Mazumder, A., and Mukherjee, G.D. (2020) Thermal conductivity of dense hcp iron: Direct measurements using laser heated diamond anvil cell. Geoscience Frontiers, 11, 1755–1761, https://doi.org/10.1016/j.gsf.2019.12.010.

Seagle, C.T., Cottrell, E., Fei, Y., Hummer, D.R., and Prakapenka, V.B. (2013) Electrical and thermal transport properties of iron and iron-silicon alloy at high pressure. Geophysical Research Letters, 40, 5377–5381, https://doi.org/10.1002/2013GL057930.

Secco, R.A. (2017) Thermal conductivity and Seebeck coefficient of Fe and Fe-Si alloys: Implications for variable Lorenz number. Physics of the Earth and Planetary Interiors, 265, 23–34, https://doi.org/10.1016/j.pepi.2017.01.005.

Secco, R.A., and Schloessin, H.H. (1989) The electrical resistivity of solid and liquid Fe at pressures up to 7 GPa. Journal of Geophysical Research, 94, 5887–5894, https://doi.org/10.1029/JB094iB05p05887.

Sha, X., and Cohen, R.E. (2011) First-principles studies of electrical resistivity of iron under pressure. Journal of Physics: Condensed Matter, 23, 075401, https://doi.org/10.1088/0953-8984/23/7/075401.

Silber, R.E., Secco, R.A., Yong, W., and Littleton, J.A.H. (2018) Electrical resistivity of liquid Fe to 12 GPa: Implications for heat flow in cores of terrestrial bodies. Scientific Reports, 8, 1–9, https://doi.org/10.1038/s41598-018-28921-w.

Uher, C. (2004) Thermal Conductivity of Metals. In T.M. Tritt, Ed., Thermal Conductivity, p. 21–91. Springer, U.S.

van der Pauw, L.J. (1958) A method of measuring specific resistivity and Hall effect of discs of arbitrary shape. Philips Research Reports, 13, 1–9.

Wagle, F., Steinle-Neumann, G., and De Koker, N. (2018) Saturation and negative temperature coefficient of electrical resistivity in liquid iron-sulfur alloys at high

densities from first-principles calculations. Physical Review B, 97, 94307–94307, https://doi.org/10.1103/PhysRevB.97.094307.

Williams, W.S. (1998) The thermal conductivity of metallic ceramics. JOM, 50, 62–66, https://doi.org/10.1007/s11837-998-0131-y.

Xu, J., Zhang, P., Haule, K., Minar, J., Wimmer, S., Ebert, H., and Cohen, R.E. (2018) Thermal conductivity and electrical resistivity of solid iron at Earth's core conditions from first principles. Physical Review Letters, 121, 96601–96601, https://doi.org/10.1103/PhysRevLett.121.096601.

Yin, Y., Zhang, Q., Zhang, Y., Zhai, S., and Liu, Y. (2022a) Electrical and thermal conductivity of Earth's core and its thermal evolution-A review. Acta Geochimica, 41, 665–688, https://doi.org/10.1007/s11631-021-00523-w.

Yin, Y., Wang, L., Zhai, S., and Fei, Y. (2022b) Electrical resistivity of Fe and Fe-3 wt%P at 5 GPa with implications for the moon's core conductivity and dynamo. Journal of Geophysical Research: Planets, 127, e2021JE007116, https://doi.org/10.1029/2021je007116.

Yokoo, S., Hirose, K., Tagawa, S., Morard, G., and Ohishi, Y. (2022) Stratification in planetary cores by liquid immiscibility in Fe-S-H. Nature Communications, 13, 644, https://doi.org/10.1038/s41467-022-28274-z.

Yong, W., Secco, R.A., Littleton, J.A.H., and Silber, R.E. (2019) The iron invariance: Implications for thermal convection in Earth's core. Geophysical Research Letters, 46, 11065–11070, https://doi.org/10.1029/2019GL084485.

Yue, S.-Y., and Hu, M. (2019) Insight of the thermal conductivity of ϵ-iron at Earth's core conditions from the newly developed direct ab initio methodology. Journal of Applied Physics, 125, 045102, https://doi.org/10.1063/1.5055389.

Zhang, C., Lin, J.F., Liu, Y., Feng, S., Jin, C., Hou, M., and Yoshino, T. (2018) Electrical resistivity of Fe-C alloy at high pressure: Effects of carbon as a light element on the thermal conductivity of the Earth's core. Journal of Geophysical Research: Solid Earth, 123, 3564–3577, https://doi.org/10.1029/2017JB015260.

Zhang, J., and Guyot, F. (1999) Thermal equation of state of iron and $Fe_{0.91}Si_{0.09}$. Physics and Chemistry of Minerals, 26, 206–211.

Zhang, Y., Hou, M., Liu, G., Zhang, C., Prakapenka, V.B., Greenberg, E., Fei, Y., Cohen, R.E., and Lin, J.F. (2020) Reconciliation of experiments and theory on transport properties of iron and the geodynamo. Physical Review Letters, 125, 78501, https://doi.org/10.1103/PhysRevLett.125.078501.

Zhang, Y., Luo, K., Hou, M., Driscoll, P., Salke, N.P., Minár, J., Prakapenka, V.B., Greenberg, E., Hemley, R.J., Cohen, R.E., and others (2022) Thermal conductivity of Fe-Si alloys and thermal stratification in Earth's core. Proceedings of the National Academy of Sciences, 119, e2119001119, https://doi.org/10.1073/pnas.2119001119.

This is the peer-reviewed, final accepted version for American Mineralogist, published by the Mineralogical Society of America.
The published version is subject to change. Cite as Authors (Year) Title. American Mineralogist, in press.
DOI: https://doi.org/10.2138/am-2023-9246. http://www.minsocam.org/

874 **Figure captions**

875 **Figure 1.** The electrical resistivity (**a**) and thermal conductivity (**b**) of iron at room
876 temperature and high pressure conditions. (**a**) shows our measured results at pressures up
877 to 26 GPa (half solid circles, U1419 and U1423) and computed results at pressures up to
878 136 GPa (solid triangles, R1 and R2). The labels exp and calc state the results from
879 experimental measurement and FPMD calculations, respectively. R1 and R2 differ on the
880 input lattice parameters, where the former applied the DFT-based lattice parameters
881 calculated at 0 K and the latter with experimental data measured at 300 K. The arrows in
882 (**a**) and (**b**) note the pressures of the bcc to hcp phase transition and the electronic
883 topological transition (ETT). In (**a**) and (**b**), we see the R1 run exhibits opposite pressure
884 dependency compared to experimental results at 80-136 GPa, indicating the failure of
885 prediction from the calculated lattice parameters at 0 K. In (**b**), all the experimental
886 thermal conductivity values are measured directly in high *P*-*T* experiments. References:
887 Ez21-(Ezenwa and Yoshino 2021); Go13-(Gomi et al. 2013); Hs20-(Hsieh et al. 2020);
888 Ja02-(Jaccard et al. 2002); Kl23-(Kleinschmidt et al. 2023); Oh18-(Ohta et al. 2018);
889 Se13-(Seagle et al. 2013); Sh11-(Sha and Cohen 2011); Zh18, Zh20-(Zhang et al. 2018,
890 2020).

891

892 **Figure 2.** The electrical resistivity (**a**) and thermal conductivity (**b**) of hcp iron at high *P*-
893 *T* conditions. In (**a**), the experimental data from Zhang et al. (2020) only display the error
894 bar at the highest temperature. Solid and dashed lines are Bloch-Grüneisen fitting lines
895 from Zhang et al. (2020). In (**b**), the numbers near the symbol note the pressures, and the
896 pressure error is in parentheses. The grey short-dashed line and region (noted as WFL)

897 show the predicted thermal conductivity range of solid hcp iron at 105 and 136 GPa via
898 the Wiedemann-Fanz law in this study, in which the resistivity data is the Bloch-
899 Grüneisen fitting data from Zhang et al. (2020), and the Lorentz number is from this
900 study. The data of grey short-dashed lines are calculated with L values of 2.20×10^{-8}
901 $W\Omega K^{-2}$ and the grey regions are calculated with L values from 2.0 to 2.4×10^{-8} $W\Omega K^{-2}$.
902 The red solid triangles state the calculated electronic thermal conductivity from this study,
903 whereas the open inverted triangles are data with an EES correction. References: Ko16-
904 (Konôpková et al. 2016); Ko19-(Korell et al. 2019); Oh23-(Ohta et al. 2023); Sa20-
905 (Saha et al. 2020); Xu18-(Xu et al. 2018); Zh20-(Zhang et al. 2020).

906

907 **Figure 3.** The Lorenz numbers of Fe at room-temperature (**a**) and high temperature (**b**)
908 conditions. (**a**) The grey horizontal dash-dot, dash-dot-dot, and dash lines represent
909 Lorenz numbers of the theoretical value (L_0 = 2.44×10^{-8} $W\Omega K^{-2}$), iron with disordered
910 lattice structure (2.28×10^{-8} $W\Omega K^{-2}$), and iron with ordered lattice structure (1.57×10^{-8}
911 $W\Omega K^{-2}$), respectively (Pourovskii et al. 2020). The experimental Lorentz number is
912 computed from experimental resistivity (Seagle et al. 2013; Zhang et al. 2020) and
913 experimental thermal conductivity (Hsieh et al. 2020; Konôpková et al. 2016; Saha et al.
914 2020) data. (**b**) Symbols of plus, cross and open square denote the Lorentz numbers after
915 electron-electron scattering (EES) correction. The black short dash and short dot curves
916 are part of the Lorentz number of hcp iron from the theoretical calculation studies by
917 Gomi and Yoshino (2018) and Pourovskii et al. (2017), respectively. The results from
918 Pourovskii et al. (2017) include the EES effect while those from Gomi and Yoshino
919 (2018) do not. Some error bars of results from this study are smaller than the symbol size.

The dash-dot line denotes the L_0 value. The inset in (**b**) shows an enlarged view of all theoretically calculated Lorentz numbers with EES correction, and the y-axis is the ratio of calculated and theoretical L. References: de12-(de Koker et al. 2012), Go18-(Gomi and Yoshino 2018), Hs20-(Hsieh et al. 2020), Ko16-(Konôpková et al. 2016), Po17-(Pourovskii et al. 2017), Sa20-(Saha et al. 2020); Se13-(Seagle et al. 2013); Xu18-(Xu et al. 2018); Zh20-(Zhang et al. 2020).

Figure 4. The thickness of the potential thermally stratified layer beneath CMB varies with the total heat flow across the CMB (Q_{cmb}). The grey dashed line is the calculated inner core age from Li et al. (2022). Open circles represent the thickness when the thermal conductivity at CMB is ~100 W/m/K from the study by Zhang et al. (2022). The vertical light-yellow area represents the most likely Q_{cmb} values at present-day CMB. Numbers next to the symbols and lines represent different thermal conductivity (70, 90, and 100 W/m/K) at CMB. Though the thermal conductivity of liquid iron is ~95-114 W/m/K at the CMB, the alloying of iron and light elements (silicon and oxygen) may reduce the thermal conductivity to 70-90 W/m/K (Pozzo et al. 2022; Li et al. 2022), and thus the most possible thermal conductivity at CMB is around 70-90 W/m/K. The black dashed area represents the thickness of thermally stratified layer beneath the CMB when the thermal conductivity at CMB varies from 70 to 90 W/m/K.

939 **Table 1.** Pressure, electrical resistivity (ρ), electronic thermal conductivity (κ_{el}), and Lorentz number (L) for hcp iron in this study.

Pressures※ (GPa)	Temperature (K)	ρ (μΩ·cm)	κ_{el} (W/m/K)	L (10^{-8} WΩK^{-2})	Pressures (GPa)	Temperature (K)	ρ (μΩ·cm)	κ_{el} (W/m/K)	L (10^{-8} WΩK^{-2})
Room temperature (300 K)									
R1*					R2				
22	-	10.65(102)	77.84(570)	2.61(13)	22	-	9.69(110)	92.82(1179)	2.73(15)
30	-	8.64(64)	99.24(950)	2.69(11)	29	-	8.13(133)	107.58(1857)	2.65(10)
40	-	8.09(58)	105.92(639)	2.67(12)	50	-	6.88(53)	115.77(743)	2.56(14)
60	-	6.14(49)	133.79(634)	2.59(15)	80	-	6.54(71)	110.64(1109)	2.35(21)
80	-	5.81(52)	127.09(1051)	2.37(11)	105	-	5.91(66)	116.58(662)	2.26(25)
100	-	6.52(72)	115.19(785)	2.43(21)	136	-	5.72(65)	128.56(844)	2.36(38)
136	-	7.66(55)	85.57(478)	2.12(10)					
High pressure-temperature									
98.5	1562	37.86(279)	105.32(737)	2.53(2)	132	2725	55.79(287)	130.20(525)	2.66(4)
98.6	3521	80.01(333)	137.33(578)	3.13(3)	134	4114	79.58(359)	157.76(840)	3.06(3)

940 ※Pressure-temperature conditions and lattice parameters are referred to Dewaele et al. (2006); Anzellini et al. (2013); and Fei et al. (2016) for iron.

941 *The lattice parameters used in R1 simulation are calculated at 0 K while R2 simulation are from experiments. All lattice parameters are listed in
942 Table S1.

Fig.1

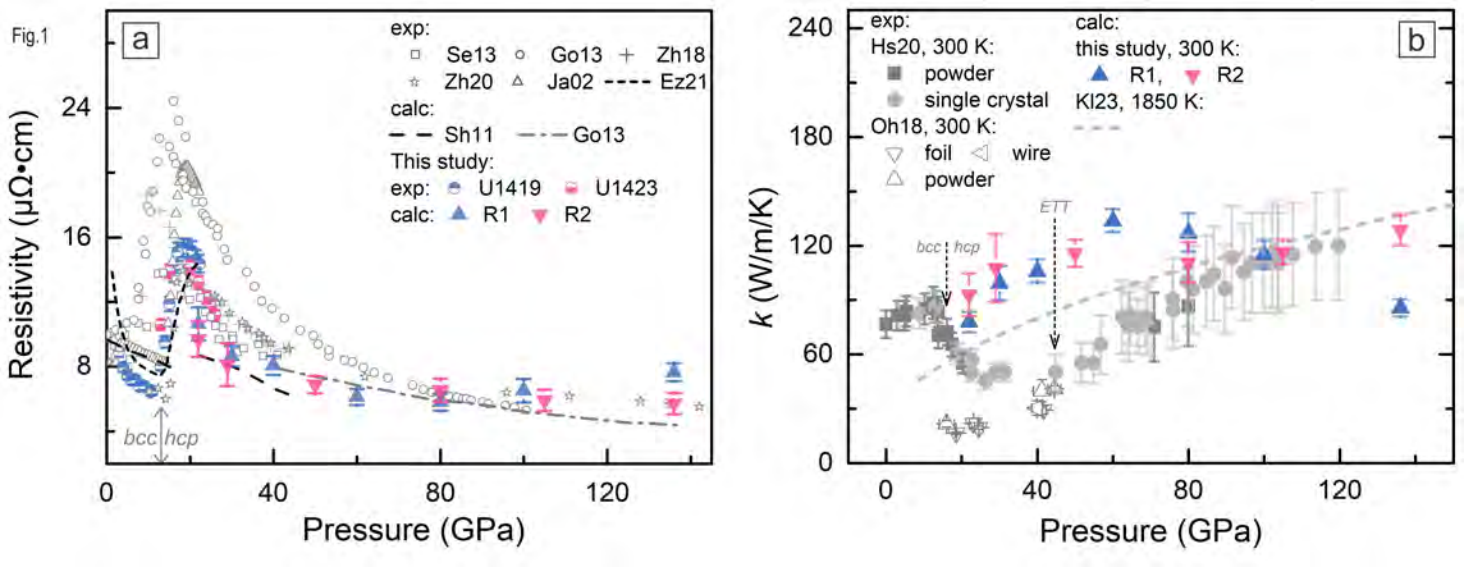
a
exp:
Se13
Go13
Zh18
Zh20
Ja02
Ez21
calc:
Sh11
Go13
This study:
exp: U1419 U1423
calc: R1 R2
Resistivity (μΩ•cm)
24
16
8
bcc
hcp
0
40
80
120
Pressure (GPa)
b
exp:
Hs20, 300 K:
powder
single crystal
Oh18, 300 K:
foil
wire
powder
calc:
this study, 300 K:
R1,
R2
Kl23, 1850 K:
ETT
bcc
hcp
k (W/m/K)
240
180
120
60
0
0
40
80
120
Pressure (GPa)

Fig.2

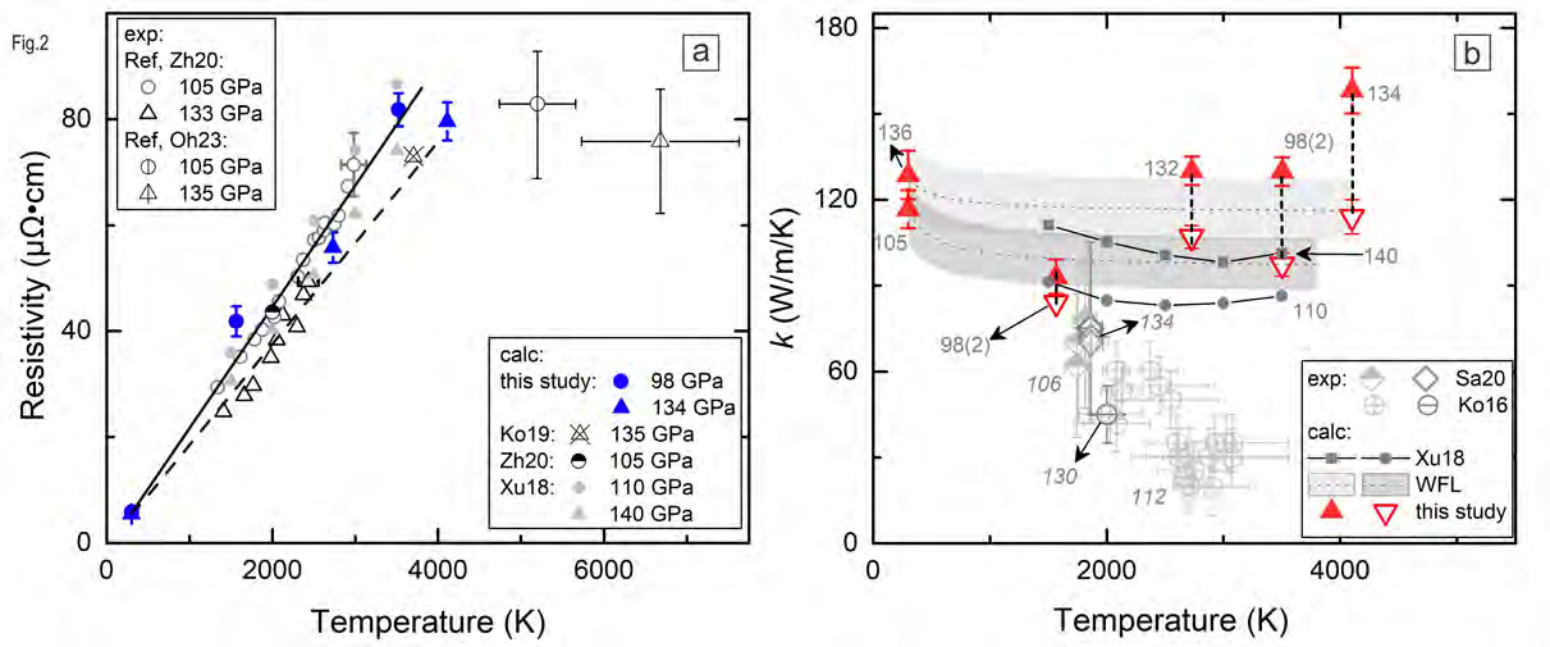
a
exp:
Ref, Zh20:
105 GPa
133 GPa
Ref, Oh23:
105 GPa
135 GPa
calc:
this study: 98 GPa
134 GPa
Ko19: 135 GPa
Zh20: 105 GPa
Xu18: 110 GPa
140 GPa
Resistivity (μΩ•cm)
Temperature (K)
b
136
105
132
98(2)
134
140
110
106
130
112
exp:
Sa20
Ko16
calc:
Xu18
WFL
this study
k (W/m/K)
Temperature (K)

Fig.3

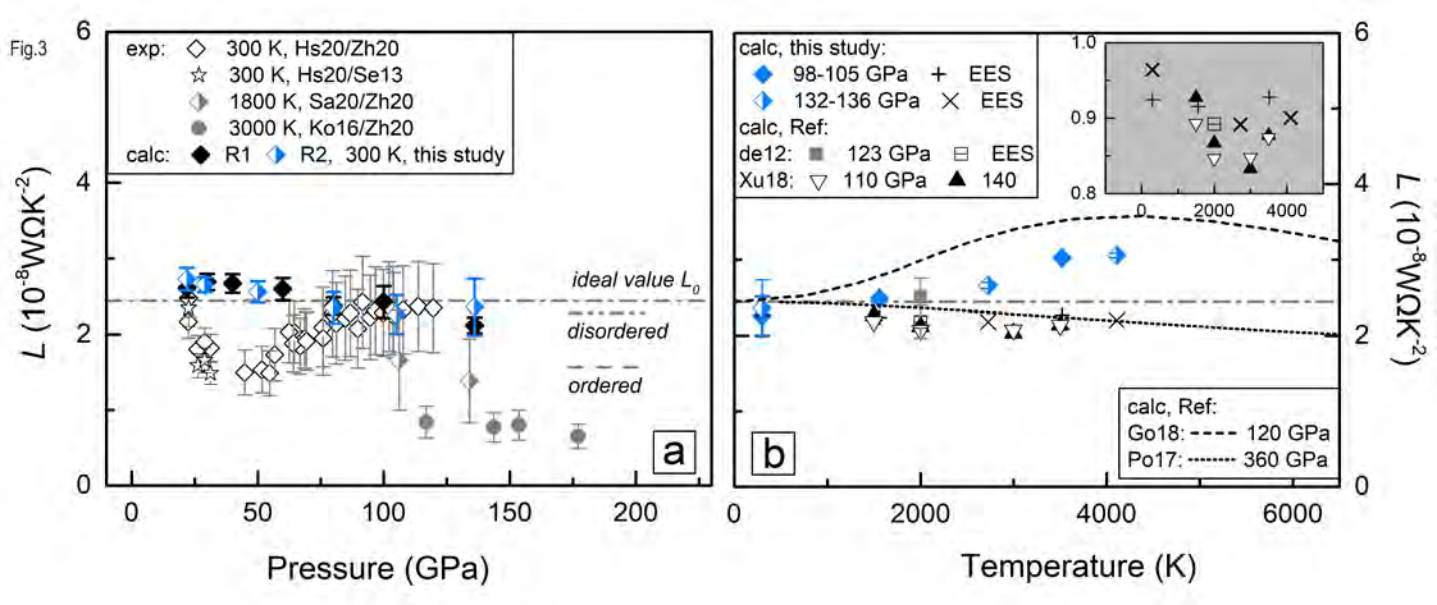
exp: 300 K, Hs20/Zh20
300 K, Hs20/Se13
1800 K, Sa20/Zh20
3000 K, Ko16/Zh20
calc: R1 R2, 300 K, this study
ideal value L_0
disordered
ordered
a
L (10^{-8}WΩK^{-2})
Pressure (GPa)
calc, this study:
98-105 GPa + EES
132-136 GPa × EES
calc, Ref:
de12: 123 GPa EES
Xu18: 110 GPa 140
calc, Ref:
Go18: 120 GPa
Po17: 360 GPa
b
Temperature (K)

Fig.4

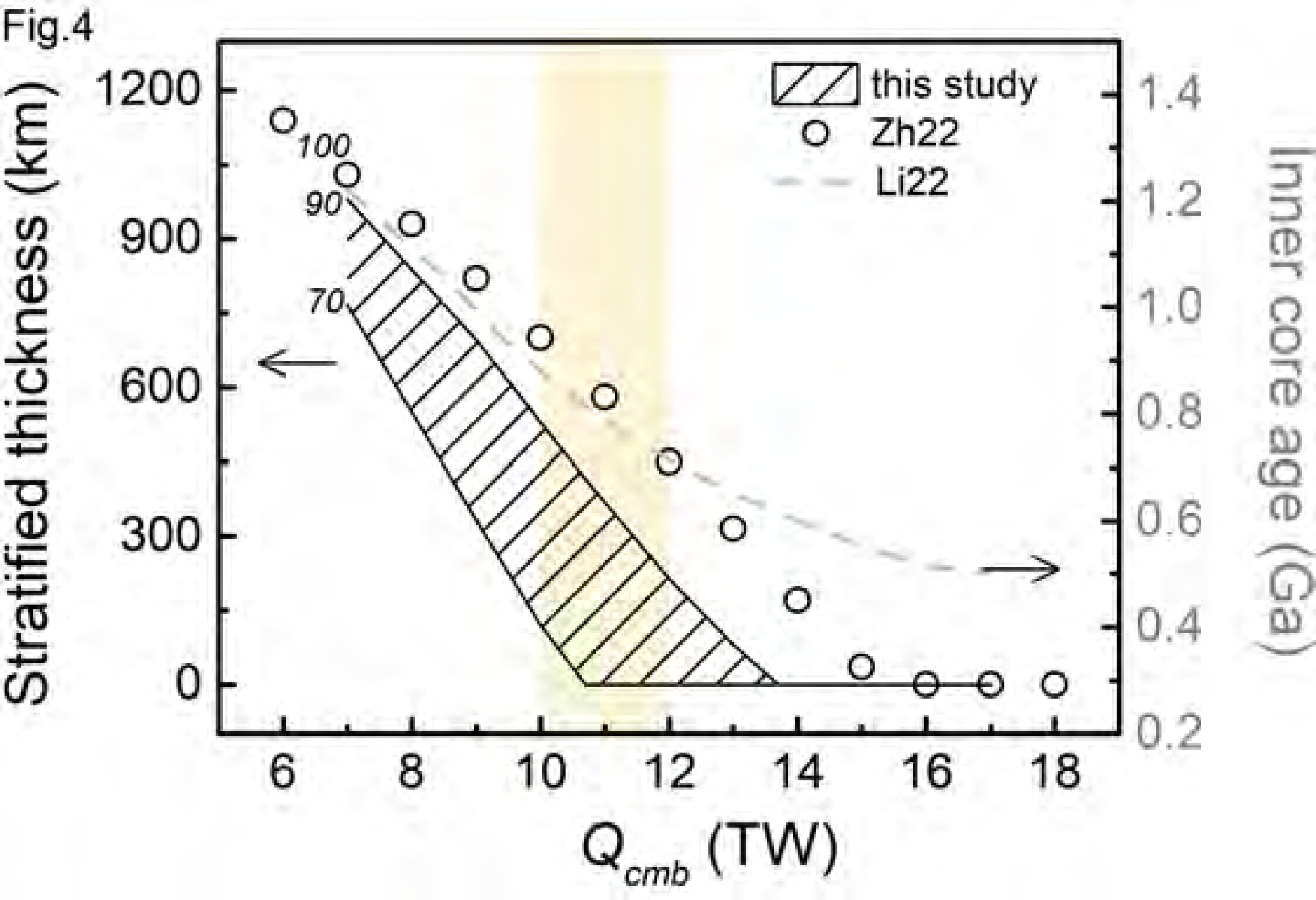
Stratified thickness (km)
1200
900
600
300
0
6
8
10
12
14
16
18
Q_{cmb} (TW)
Inner core age (Ga)
1.4
1.2
1.0
0.8
0.6
0.4
0.2
this study
Zh22
Li22
100
90
70